*Sensors and Materials*, Vol. 37, No. 2 (2025) 717–726
MYU Tokyo



S & M 3951

# Geometric Positioning Accuracy Improvement of 1-meter C-band Synthetic Aperture Radar 01 Satellite Images

Yufan Sun[1] and Maoqiang Jing[2*]

[1]School of Remote Sensing and Information Engineering, Wuhan University, Wuhan 430072, China
[2]State Key Laboratory of Information Engineering in Surveying, Mapping and Remote Sensing, Wuhan University, Wuhan 430072, China

(Received October 25, 2024; accepted February 6, 2025)

***Keywords:*** synthetic aperture radar, C-SAR, Gaofen-3, absolute positioning accuracy, geolocation validation

The 1-meter C-SAR 01 satellite (C-SAR), launched on November 23, 2021, is a C-band high-resolution synthetic aperture radar (SAR) satellite launched by China, similar to Gaofen-3. The images acquired by this satellite are widely used to study land and marine resources. Geometric positioning accuracy is an important index to evaluate the quality of SAR images. In this study, we aimed to evaluate the positioning accuracy of L1A standard products of the C-SAR satellite and determined possible improvements. We used the high-precision calibrator equipment of the Zhongwei calibration field as the checkpoint to evaluate the positioning accuracy of the five image modes of the C-SAR satellite: FSI, FSII, QPSI, QPSII, and SS. Additionally, we used a series of accuracy improvement methods, including azimuth time correction under the "stop-and-go" approximation, atmospheric propagation delay correction, and geometric calibration for the error source of the whole positioning link. We evaluated the positioning accuracy of the improved images. The test results showed that the positioning accuracy of the C-SAR satellite images can be improved to approximately 4 m.

## 1. Introduction

On November 23, 2021, China successfully launched the 1-meter C-SAR 01 satellite from Jiuquan Satellite Launch Center. This satellite is the first operational synthetic aperture radar (SAR) satellite launched by China, which indicates that China's SAR satellite strategy has transitioned from performing scientific experiments to special applications. The satellite further improves China's marine remote sensing operational observation capability. The imaging modes of C-SAR (Table 1) are consistent with that of Gaofen-3, which has been in orbit for six years.(1) One of the key problems in the application of SAR remote sensing is the geometric positioning of SAR images, that is, the determination of the mathematical relationship between the SAR image pixels and the target geographical location through SAR imaging geometry, which is performed after the SAR image has been focused.(2) The accuracy of geometric positioning has

*Corresponding author: e-mail: jingmq@whu.edu.cn
https://doi.org/10.18494/SAM5411

ISSN 0914-4935 

Table 1
C-SAR satellite information.

| Item | | Parameter | | |
|---|---|---|---|---|
| Weight of satellite | | 2950 kg | | |
| Design life | | 8 years | | |
| Orbit altitude | | 755 km | | |
| Band | | C | | |
| Range of incidence angle | | ~10–60° | | |
| Imaging mode | | Resolution (m) | Image width (km) | Polarization |
| Sliding spotlight | | 1 | 10 | Single |
| Strip | Ultrafine strip | 3 | 30 | Single |
| | Fine strip 1 | 5 | 50 | Dual |
| | Fine strip 2 | 10 | 100 | Dual |
| | Standard strip | 25 | 130 | Dual |
| | Quad polarization strip 1 | 8 | 30 | Full |
| | Quad polarization strip 2 | 25 | 40 | Full |
| TOPSAR | Narrow scan | 50 | 300 | Dual |
| | Wide scan | 100 | 500 | Dual |
| | Global observation | 500 | 650 | Dual |
| Wave imaging | | 8 | 20 | Full |
| Extended incident angle | Low | 25 | 130 | Dual |
| | High | 25 | 80 | Dual |

become the main factor restricting the application of SAR images and is an important index to evaluate their quality.[3]

The C-SAR standard products were divided into three levels: L1A, L1B, and L2. Standard product classifications and definitions are shown in Table 2. L1A standard products are the products without geometric correction. Verifying and improving the geometric positioning accuracy of L1A standard products have always been important components of SAR satellite image processing. Internationally, spaceborne SAR systems worldwide have gained good experience in performing this. ERS-1 was the first SAR satellite in the world to achieve high-precision geometric processing. After geometric calibration, the plane positioning accuracy of a single image from ERS-1, without control points, reached 10 m.[4] The positioning verification results of RADARSAT-2 imaging products from June 2008 to July 2010 showed that the positioning accuracy was improved from higher than 50 m to higher than 15 m after geometric calibration in 2009.[5] Since then, the German TerraSAR-X/Tandem-X satellite and the European Space Agency Sentinel-1A/B satellite have stabilized the positioning accuracy of imaging products at the meter level or even submeter level after high-precision geometric processing, thereby pushing the geometric positioning accuracy of spaceborne SAR images to an unprecedented level and considerably expanding the application range of spaceborne SAR images.[6–8]

In recent years, China's spaceborne SAR technology has developed rapidly. The products of Gaofen-3 have been verified in some areas, and the geometric positioning accuracy has been shown to reach 3 m or less.[9,10] Currently, C-SAR has been in orbit for over two years. The validation and evaluation of the geometric accuracy of its image products and the provision of a reference for satellite developers and product users have both scientific and practical values.

Table 2
Standard product classifications and definitions.

| Product Level | Product Form | Definition |
|---|---|---|
| L1A | Single Look Complex (SLC) Product | Slant range complex data products obtained after imaging processing and relative radiation correction according to satellite parameters |
| L1B | Single Look Power Product | Power image based on L1A SLC product |
| L2 | System Geometry Correction Product | The system-level geometric correction product is obtained after geolocation, map projection, and resampling based on the attitude and orbit data. |

Considering the above problems, in this study, we established a geometric positioning model of C-SAR based on the Range–Doppler (RD) imaging principle. On this basis, geometric positioning accuracy improvement methods such as azimuth time correction under the "stop-and-go" approximation, atmospheric path delay correction, and geometric calibration were adopted, combined with the characteristics of the C-SAR satellite system. Finally, a geometric positioning accuracy validation test was carried out using the multiple C-SAR L1A standard products over the Zhongwei calibration field.

## 2. Geometric Positioning Model and Accuracy Improvement Method for C-SAR

### 2.1 RD positioning model

The RD model is the mainstream spaceborne SAR image geometric positioning model that describes the mathematical relationship between image plane coordinates and actual spatial coordinates.[11] The image plane coordinates of the target can be obtained by the indirect positioning method of the RD model.[12] The mathematical expression of the indirect positioning method is shown in the following formula:

$$\begin{cases} R = R_{near} - \Delta L + \Delta r + i\dfrac{c}{2f_s} \\ \eta_p = \eta_0 + \Delta t_a + \dfrac{j}{PRF} \end{cases}, \tag{1}$$

where $R$ is the slant range between the SAR antenna phase center and the target; $R_{sc}$ and $V_{sc}$ represent the position ($X_s$, $Y_s$, $Z_s$) and velocity ($X_v$, $Y_v$, $Z_v$) vectors of the SAR satellite, respectively; the position vector ($X_t$, $Y_t$, $Z_t$) of the ground target is expressed by $R_{tc}$; $f_D$ represents the Doppler center frequency; and $\lambda$ represents the wavelength.

### 2.2 Methods for improving geometric positioning accuracy

As the geometric positioning parameters in Eq. (1) are not completely accurate, there is a deviation between the measured coordinates and the real coordinates of the target in the image.

By analyzing the positioning error sources of the C-SAR satellite, the geometric positioning accuracy of the C-SAR L1A standard product can be improved by the following three methods.

### 2.2.1 Azimuth time correction under "stop-and-go" approximation

The establishment of the RD model is based on a "stop-and-go" approximation. It is assumed that the SAR does not move during the transmission and reception of a single pulse, which is inconsistent with the actual physical process. During the propagation of the SAR pulse, the SAR satellite continues to move forward. When the pulse is transmitted and received, the position of the SAR satellite is different. C-SAR satellite images provide the time stamp of the image start line in the auxiliary file to allow the satellite position at that time to be calculated. This time stamp $\eta_{0r}$ corresponds to the reception time of the echo. With $\eta_{0t}$ to indicate the pulse transmission time, the relationship between $\eta_{0t}$ and $\eta_{0r}$ satisfies the following formula:

$$\eta_{0t} = \eta_{0r} - (2R_{near} + i \cdot c / f_s) / c \,, \tag{2}$$

where $R_{near}$ is the slant range of the first range gate determined by the radar pulse propagation time, $i$ is the range pixel coordinate of the target in the image, $c$ is the propagation velocity of microwaves in the atmosphere, and $f_s$ is the sampling frequency of the pulse.

The positioning error caused by the "stop-and-go" approximation can be eliminated by adjusting the azimuth imaging time of the image start line to the intermediate time between the transmission and reception of the radar observation signal.[10] Thus,

$$\eta_0 = \frac{(\eta_{0t} + \eta_{0r})}{2} = \eta_{0r} - \frac{R_{near}}{c} + \frac{i}{2f_s} \,. \tag{3}$$

### 2.2.2 Atmospheric propagation delay correction

The spaceborne SAR system calculates the slant range by recording the transit time of the radar observation signal between the antenna phase center and the ground target point. The propagation delay of the radar observation signal in the atmosphere will trigger an error in slant-range measurement. The atmospheric delay correction method based on external data can be used to calculate the atmospheric delay correction value. The atmospheric delay correction model is as follows:

$$\Delta L = \frac{1}{\cos(\varepsilon)} \Delta L_Z \,, \tag{4}$$

where $\varepsilon$ is the incidence angle and $\Delta L_Z$ is the atmospheric zenith delay.

The calculation of the atmospheric zenith delay $\Delta L_Z$ is divided into two parts: the tropospheric zenith delay $\Delta L_{trop}$ and ionospheric zenith delay $\Delta L_{iono}$. The calculation formula for $\Delta L_{trop}$ is as follows:

$$\begin{cases} \Delta L_{trop} = \int_z^{\infty} (n(z)-1)dz \\ (n(z)-1) = 10^{-6} N \\ N = k_1(\lambda)\dfrac{P_d}{T} z_d{}^{-1} + k_2(\lambda)\dfrac{P_w}{T} z_w{}^{-1} \end{cases}, \tag{5}$$

where $z$ is elevation, $n(z)$ is the refractive index along the zenith direction, $P_d$ is the pressure of dry air, $T$ is temperature, $z_d$ is the compressibility of dry air, $P_w$ is the pressure of wet air, and $z_w$ is the compressibility of wet air. $k_1(\lambda)$ and $k_2(\lambda)$ are related to the wavelength of the radar signal, $\lambda$.

In this study, we used the atmospheric analysis model of the American National Center for Environmental Prediction as the external data. The empirical equations proposed by Owens for $k_1(\lambda)$ and $k_2(\lambda)$ are as follows:[13]

$$\begin{cases} k_1(\lambda) = 0.237134 + 68.39397\dfrac{130+\lambda^{-2}}{(130-\lambda^{-2})^2} + 0.45473\dfrac{38.9+\lambda^{-2}}{(38.9-\lambda^{-2})^2} \\ k_2(\lambda) = 0.648731 + 0.0174174\lambda^{-2} + 3.5575\lambda^{-4} + 6.1957\lambda^{-6} \end{cases}. \tag{6}$$

The calculation formula for $\Delta L_{iono}$ is as follows:

$$\Delta L_{iono} = \frac{40.28}{f^2} TEC, \tag{7}$$

where $f$ is the SAR signal frequency and TEC is the total ionospheric electron concentration.

The European Center for Orbit Determination provides global ionospheric TEC maps in Ionosphere Exchange file format. The time interval is 1 h, with a longitude interval of 5° and a latitude interval of 2.5°. The longitude range is −180° W to 180° E, the latitude range is 87.5° S to −87.5° N, and there are 5183 grid points, achieving ionospheric grid division. Therefore, the bilinear interpolation principle is first used for the TEC value at a specific time and location to interpolate the TEC content of adjacent known epochs in the four-corner grid space. Then, the linear interpolation of time is performed.

### 2.2.3 Geometric calibration

Among the error factors of image positioning accuracy, two factors are stable: the systematic azimuth time shift between the radar time and the orbit time and the slant-range deviation caused by the internal electronic delay of the instrument. The internal electronic delay error is related to the bandwidth and pulse width. Using the calibration parameters to compensate for other images' slant range and azimuth time can improve the geometric positioning accuracy. The following geometric calibration model can calibrate the correction values of these two errors:

$$\begin{cases} R = R_{near} - \Delta L + \Delta r + i\dfrac{c}{2f_s} \\ \eta_p = \eta_0 + \Delta t_a + \dfrac{j}{PRF} \end{cases}, \tag{8}$$

where $\Delta r$ and $\Delta t_a$ represent the slant-range correction and systematic azimuth shifts, respectively; $j$ is the azimuth pixel coordinate of the point target in the image; $PRF$ is the SAR pulse repetition frequency; and $R$ and $\eta_p$ are calculated by the indirect positioning method of the RD model using the ground coordinates of control points.

### 2.2.4 Evaluation index of geometric positioning accuracy

The geometric positioning accuracy evaluation of L1A standard products is generally carried out in the image plane coordinate system. Suppose an image uses N checkpoints to quantitatively evaluate the geometric positioning accuracy, and each checkpoint corresponds to two two-dimensional vectors. A vector $C_c = [X_c, Y_c]^T$ represents the image plane coordinate of the checkpoint calculated on the basis of the indirect positioning method of the RD model, and another vector $C_r = [X_r, Y_r]^T$ represents the true value of the image plane coordinate corresponding to the checkpoint. The error vector $E = [E_X, E_Y]^T$ of a checkpoint is calculated as

$$E = C_c - C_r . \tag{9}$$

The positioning accuracy of an image is obtained by determinig the root mean square error of all N checkpoints of the image as follows:

$$E_{rms} = \sqrt{\frac{1}{N}\sum_{i=1}^{N} E_i^2} . \tag{10}$$

## 3. Experiments and Discussion

### 3.1 Experimental data

The Zhongwei remote sensing satellite calibration field, a hilly area with an altitude of 1100–2955 m (Fig. 1), was selected as the test area. This area was equipped with 20 corner reflectors (CR), each with a side length of 1 m, and three active radar calibrators (ARCs), which can be used for high-precision checkpoint data. Global navigation satellite system real-time kinematic technology was used to obtain the accurate ground coordinates of 23 equipment items, and the measurement accuracy reached the centimeter level. The appearance of the ARC on the SAR image is shown in Fig. 2. The coordinates of the control point on the image were also easy to identify, and the extraction accuracy was higher than 0.5 pixels.

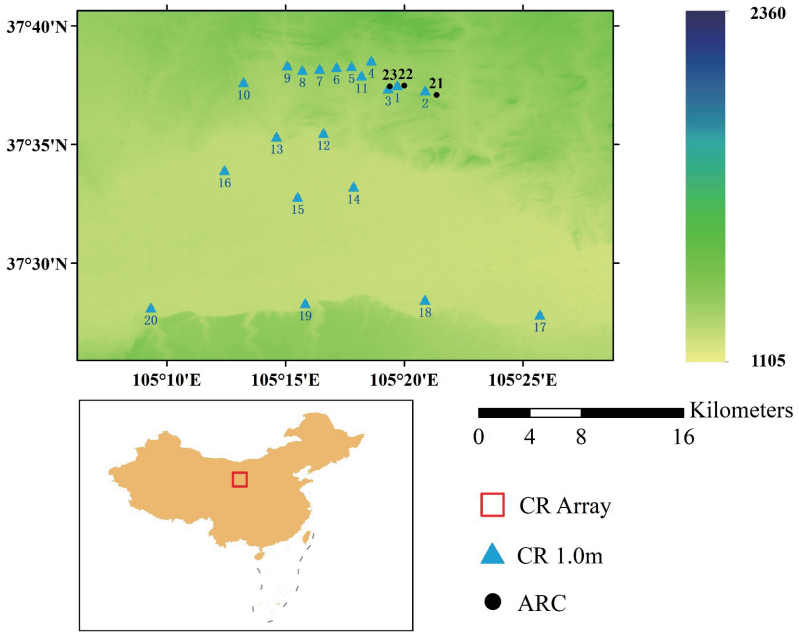


Fig. 1. (Color online) Zhongwei remote sensing satellite calibration field.

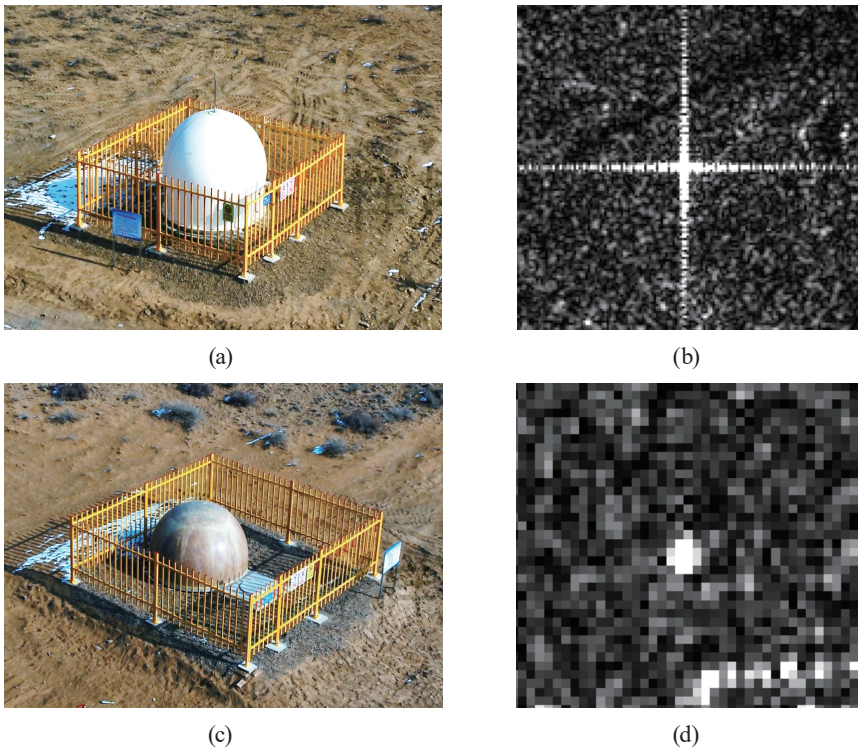

(a) (b)

(c) (d)

Fig. 2. (Color online) Checkpoint information. (a) On-site photo of ARC. (b) ARC on SAR image. (c) On-site photo of CR. (d) CR on SAR image.

Data from 12 C-SAR satellite images were acquired in this area from five imaging modes: FSI, FSII, QPSI, QPSII, and SS. The specific information of each image is provided in Table 3. Two images are listed under each bandwidth and pulse width combination: one as the calibration image and the other as the verification image.

### 3.2 Test scheme design

We compared and verified the effectiveness of the proposed C-SAR geometric accuracy improvement method. The following schemes were used for comparison tests:

Scheme 1: The positioning accuracy of the validation image in Table 1 is directly evaluated without any improvement;

Scheme 2: For the validation images in Table 1, only the "stop-and-go" approximation was carried out to evaluate the positioning accuracy;

Scheme 3: On the basis of scheme 2, the atmospheric propagation delay of the image was corrected, and the positioning accuracy of the validation images in Table 1 was verified;

Scheme 4: On the basis of scheme 3, the geometric calibration parameters obtained from the calibration image in Table 1 were used to compensate for the validation image in Table 1. The positioning accuracy of the image after compensation was verified.

### 3.3 Results and analysis

The comparative test of the positioning accuracy of C-SAR was carried out according to the test scheme described in the previous section. The positioning accuracies of the validation images under each scheme are listed in Table 4.

The comparison of the results of schemes 1 and 2 shows that the azimuth positioning accuracy of the image was considerably improved by correcting the azimuth time error under the "stop-and-go" approximation. The level of improvement of the azimuth positioning accuracy

Table 3
Test data information.

| Imaging mode | Resolution (m) | Image ID | Bandwidth (MHz) & pulse width (μs) | Image properties | Imaging date | Orbit & lookside | Incidence angle (°) |
|---|---|---|---|---|---|---|---|
| FSI | 5 | FSI_001268 | 60 & 30 | Calibration | February 18, 2022 | Desc & L | 28.5 |
| | | FSI_001852 | 60 & 30 | Validation | March 31, 2022 | Asc & L | 36.0 |
| FSII | 10 | FSII_001513 | 60 & 50 | Calibration | March 07, 2022 | Desc & L | 35.1 |
| | | FSII_001607 | 60 & 50 | Validation | March 14, 2022 | Asc & L | 39.1 |
| | | FSII_001579 | 100 & 45 | Calibration | March 12, 2022 | Asc & L | 20.2 |
| | | FSII_001614 | 100 & 45 | Validation | March 14, 2022 | Desc & L | 20.2 |
| QPSI | 8 | QPSI_001362 | 30 & 25 | Calibration | February 25, 2022 | Asc & L | 42.2 |
| | | QPSI_001830 | 30 & 25 | Validation | March 29, 2022 | Desc & L | 42.7 |
| QPSII | 25 | QPSII_001686 | 40 & 20 | Calibration | March 19, 2022 | Desc & L | 29.0 |
| | | QPSII_001931 | 40 & 20 | Validation | April 05, 2022 | Desc & L | 34.2 |
| SS | 25 | SS_001441 | 40 & 50 | Calibration | March 02, 2022 | Desc & L | 24.1 |
| | | SS_002169 | 40 & 50 | Validation | April 22, 2022 | Asc & L | 24.1 |

Desc = Descending; Asc = Ascending; L = Left; R = Right.

Table 4
Validation image positioning accuracy results.

| Imaging mode | Bandwidth (MHz) & pulse width (μs) | Image ID | Scheme | Positioning accuracy | | |
|---|---|---|---|---|---|---|
| | | | | Azimuth (m) | Range (m) | Plane (m) |
| FSI | 60 & 30 | FSI_001852 | 1 | 18.507 | 22.249 | 28.940 |
| | | | 2 | 3.205 | 22.249 | 22.479 |
| | | | 3 | 3.205 | 19.132 | 19.399 |
| | | | 4 | 0.719 | 3.534 | 3.606 |
| FSII | 60 & 50 | FSII_001607 | 1 | 21.630 | 23.912 | 32.244 |
| | | | 2 | 1.695 | 23.912 | 23.972 |
| | | | 3 | 1.695 | 20.585 | 20.654 |
| | | | 4 | 1.300 | 2.490 | 2.809 |
| | 100 & 45 | FSII_001614 | 1 | 14.212 | 16.303 | 21.628 |
| | | | 2 | 4.241 | 16.303 | 16.845 |
| | | | 3 | 4.241 | 13.775 | 14.413 |
| | | | 4 | 2.953 | 1.580 | 3.349 |
| QPSI | 30 & 25 | QPSI_001830 | 1 | 21.122 | 21.477 | 30.124 |
| | | | 2 | 3.387 | 21.477 | 21.742 |
| | | | 3 | 3.387 | 17.916 | 18.233 |
| | | | 4 | 0.884 | 0.778 | 1.178 |
| QPSII | 40 & 20 | QPSII_001931 | 1 | 16.475 | 30.661 | 34.807 |
| | | | 2 | 4.674 | 30.661 | 31.015 |
| | | | 3 | 4.674 | 27.707 | 28.098 |
| | | | 4 | 1.302 | 0.415 | 1.366 |
| SS | 40 & 50 | SS_002169 | 1 | 14.797 | 19.788 | 24.709 |
| | | | 2 | 4.404 | 19.788 | 20.272 |
| | | | 3 | 4.404 | 17.157 | 17.714 |
| | | | 4 | 3.876 | 1.304 | 4.089 |

differed across different validation images; this is mainly because the time error caused by the "stop-and-go" approximation is related to the slant range in the imaging geometry according to Eq. (3). Different images have different angles of incidence, orbits, and other conditions when shooting; therefore, there are certain differences in slant-range values.

The comparison of the results of schemes 2 and 3 shows that the range positioning accuracy of the image was improved to a certain extent by correcting the atmospheric delay, and the deviation in range positioning caused by the atmospheric delay was approximately 3 m, verifying the effectiveness of the proposed atmospheric delay correction method.

The comparison of the results of schemes 3 and 4 shows that the azimuth time and slant-range correction values were obtained by geometric calibration, and the validation image was compensated. The range positioning accuracy of the verification image was considerably improved, and the azimuth positioning accuracy was slightly improved.

According to the results of the positioning accuracy evaluation of the four schemes, the proposed processing methods are effective. After processing, the positioning accuracy of C-SAR images is generally 4 m or less.

## 4. Conclusion

In this study, we used a series of geometric accuracy improvement methods for C-SAR images, including azimuth time correction under the "stop-and-go" approximation, atmospheric propagation delay correction, and geometric calibration. From the experimental results and analysis, the following conclusions can be drawn.

1) Without improvement, the different modes of the C-SAR satellite are identical in their accuracy. After processing, the positioning accuracy of the image is 4.089 m or higher and can even reach 1.178 m in a good situation, which is equivalent to the accuracy of international advanced satellites.
2) According to the analysis of the source of positioning error, the azimuth time error caused by the "stop-and-go" approximation is the main error source of positioning for the azimuth direction; for the range direction, the slant-range measurement error caused by the internal electronic delay of the instrument is the main error source of positioning.

## Acknowledgments

This work was sponsored by the National Key Research and Development Program of China (2023YFB3905503).

## References

1 N. Jiao, F. Wang, H. You, and X. Qiu: IEEE Geosci. Remote Sens. Lett. **17** (2019) 1747. https://doi.org/10.1109/LGRS.2019.2955491
2 J. C. Curlander and R. N. McDonough: Synthetic Aperture Radar: Systems and Signal Processing (John Wiley & Sons, New York, 1991).
3 T. Wang, G. Zhang, L. Yu, R. Zhao, M. Deng, and K. Xu: Sensors **17** (2017) 2005. https://doi.org/10.3390/s17092005
4 J. J. Mohr and S. N. Madsen: IEEE Trans. Geosci. Remote Sens. **39** (2001) 842. https://doi.org/10.1109/36.917909
5 S. Srivastava, S. Cote, S. Muir, and R. Hawkins: IEEE Int. Geosci. Remote Sens. Sympos. (2010) 3458. https://doi.org/10.1109/IGARSS.2010.5650129
6 U. Balss, C. Gisinger, and M. Eineder: Remote Sens. **10** (2018) 656. https://doi.org/10.3390/rs10040656
7 A. Schubert, N. Miranda, D. Geudtner, and D. Small: Remote Sens. **9** (2017) 607. https://doi.org/10.3390/rs9060607
8 C. Gisinger, A. Schubert, H. Breit, M. Garthwaite, U. Balss, M. Willberg, D. Small, M. Eineder, and N. Miranda: IEEE Trans. Geosci. Remote Sens. **59** (2020) 1154. https://doi.org/10.1109/TGRS.2019.2961248
9 R. Zhao, Z. Guo, M. Deng, K. Xu, and F. Guo: Sensors **17** (2017) 1977. https://doi.org/10.3390/s17091977
10 M. Deng, G. Zhang, C. Cai, K. Xu, R. Zhao, F. Guo, and J. Suo: Remote Sens. **11** (2019) 1465. https://doi.org/10.3390/rs11121465
11 J. C. Curlander: IEEE Trans. Geosci. Remote Sens. (1982) 359. https://doi.org/10.1109/TGRS.1982.350455
12 X. Liu, H. Ma, and W. Sun: Advances in Machine Vision, Image Processing, and Pattern Analysis. Lecture Notes in Computer Science, Eds. N. Zheng, X. Jiang, and X. Lan (Springer, Berlin, Heidelberg, 2006).
13 J. C. Owens: Appl. Optics. **6** (1967) 51. https://doi.org/10.1364/AO.6.000051